Compact Design of 40 kV 100 A High-Voltage Pulsed-Power Modulator for Driving X-Band Magnetrons

Hyun-Bin Jo, Jae-Beom Ahn, Woo-Cheol Jeong, Joo-Young Lee, Min-Kyu Choi, and Hong-Je Ryoo, *Senior Member, IEEE*

***Abstract*—This article describes the design of a very compact high-voltage pulsed power modulator for application in a medical linear accelerator. This modulator is manufactured with a modular cell structure based on a semiconductor switch, and the heat dissipation structure is minimized through a simple and efficient charge-and-discharge circuit design. In addition, an equalized charging strategy for multiple capacitors and a high-voltage electric field noise reduction strategy was applied. Thus, a high voltage pulsed-power modulator with a very compact size (310 (W) mm × 480 (H) mm × 230 (D) mm) and a high peak power density of 111 kW/L was realized without the use of an external cooling device such as a chiller. The modulator was built and experiments were conducted on high-voltage noninductive resistive load outputs. The results show that the modulator had a stable pulse voltage under various conditions, such as an output voltage of up to −40 kV, an output current of up to 100 A, a variable pulse width of 2–10 μs, and an output repetition rate of up to 1 kHz. In addition, the high-voltage insulation reliability of the proposed modulator and its applicability to magnetron loads were verified.**

***Index Terms*—Compact design, gate driver design, high voltage pulsed power, linear particle accelerator (LINAC), magnetron, pulse generators, solid state pulsed-power modulator, X-band magnetron.**

I. Introduction

A LINEAR accelerator (LINAC) is a system that accelerates ions or particles along a linear beamline. It is used in a variety of applications, including microwaves in medical treatment, space, and industry. Medical LINACs are widely used for the treatment of cancer patients using radiation [1], [2], [3]. The construction of a compact and lightweight LINAC system to mount LINAC to the GANTRY of O-ARM or C-ARM type has been presented in recent studies [4], [5]. In addition, the development of compact high-voltage pulsed power modulators for driving RF power sources (such as magnetrons) of LINACs for medical use is also being promoted. Switches used in modulators are divided into mechanical and semiconductor switches. For high-voltage pulse power modulators based on mechanical switches, a pulse-shaping method such as pulse forming network is widely used [6], [7], which makes it difficult to design a compact and lightweight design owing to the need for greater cooling parts due to the low efficiency of 40%–60%. The mechanical switch's low pulse quality and short lifespan are also highlighted as major drawbacks. On the other hand, semiconductor switches have a long lifespan and allow for high-quality pulse waveform generation as well as a compact and lightweight design.

However, stacking numerous switches is problematic because of the single-switch rating limitation. Various stacking strategies have been employed for semiconductor switches to address this problem. The high-voltage direct switching technique [8], [9], which delivers a high-voltage capacitor voltage directly to the load through switches stacked in series, has a simple structure and is easy to control. However, it has a significant risk of switch avalanche failure owing to switch-driving timing problems. The solid-state switch-based MARX technique [10] is a typical topology in high-voltage pulse modulators that generates pulses by charging capacitors in parallel and then discharging them in series via switching. However, owing to the larger heat-dissipation component resulting from the low charging efficiency, the compact design is limited. Furthermore, when developing a high-voltage pulse modulator, the gate of the stack switch must be isolated from the bottom to the top of the stack, necessitating several tens of kilovolts of isolation for the gate driver. The optical signal driving technique [11], [12], which is widely used as a gate driving method, provides each driver with an isolated signal; however, each driver requires its own power source, which restricts the design of a compact modulator.

In this work, we developed several innovative design and construction strategies to build a compact high-voltage pulse power modulator for X-BAND LINACs. The modular cell-type pulse modulator [13], [14], [15] for this study can deliver isolated and synchronized gate signals to each stacked switch without a separate power source through a simple isolated control circuit using several transformers. To provide isolation between stacked

Manuscript received 19 June 2022; revised 30 September 2022 and 10 January 2023; accepted 4 February 2023. Date of publication 3 April 2023; date of current version 20 April 2023. This work was supported in part by the National Research Foundation of Korea (NRF), Korea Government (MSIP) under Grant NRF2020R1A2C2099663, in part by the Institute of Information & Communications Technology Planning & Evaluation (IITP), Korea Government (MSIT) under Grant 2022-0-00100, and in part by the Development of High Power Electromagnetic Wave based Anti-Drone System. Recommended for publication by Associate Editor Z. Zhang. *(Corresponding author: Hong-Je Ryoo.)*

The authors are with the Energy Systems Engineering, Chung-Ang University, Seoul 06082, Korea (e-mail: dlood89@cau.ac.kr; woqja0725@cau.ac.kr; dncjf94@cau.ac.kr; ilovegee@cau.ac.kr; showman5190@cau.ac.kr; hjryoo@cau.ac.kr).

Color versions of one or more figures in this article are available at https://doi.org/10.1109/TPEL.2023.3244410.

Digital Object Identifier 10.1109/TPEL.2023.3244410

modules without the use of insulating oil, a 100 kV high-voltage insulated wire with a diameter of 17 mm was utilized as the single-turn primary winding of the charging transformer in this modulator. Because the primary winding of a single turn passes through the multicore and charges 48 capacitors, a new strategy is used to reduce the multicapacitor voltage balance error caused by the magnetic flux differences of the transformers. We used special construction strategies to enhance transient immunity and eliminate unintentional malfunctions caused by high-voltage electric field interference noise and design the minimized gate driver.

We then designed and built a −40 kV 100 A pulse power modulator with a very compact size of 36 L (310 mm × 480 mm × 240 mm) and a high peak power density of 133 kW/L based on the optimized structure of the charge/discharge and control circuits. This study presents our compact modulator design technique and describes the experiments that were conducted on high-voltage noninductive resistive loads targeting the X-BAND magnetron. The design stability and outstanding performance of the high-voltage insulation of a modulator with a compact size of 36 L were verified during the modulator's maximum rating test and experiments under various conditions.

II. Proposed Structure of Compact Pulse Modulator

A. Target Design Specification

The target design specifications for the high-voltage pulse modulator utilized as a power source for driving the X-band magnetron and the LINAC RF power source for medical applications are as follows:

1) −40 kV maximum pulse output voltage;
2) Pulse output current maximum of 100 A;
3) Volume of modulator: less than 40 L;
4) Pulse droop rate of less than 5% (based on the rated output voltage and current);
5) Pulse width: 1–10 μs;
6) 1 kHz maximum repetition rate.

Accordingly, a compact high-voltage pulse modulator with a solid-state switch-based modular cell structure was designed and manufactured.

B. Compact Structural Design of −40 kV 100 A Pulse Modulator

Fig. 1 shows the schematic circuit of the designed pulse modulator. The capacitor charging part of the circuit begins on the top-left side of the circuit and is powered by single-phase ac power. It contains a high-frequency full-bridge inverter (SP1–SP4), *LCC* resonance tank (Lr, Crs, and Crp), and rectifier circuit, which is connected to six modules through 12 charging power transformers (Tpx1–Tpx12). Twelve high-voltage toroidal cores with epoxy insulation were employed as charging transformers, each with four secondary-side multiple windings. The charging power loop (Loop_pow) is the primary winding that passes through these transformers, and its cable is a 100 kV insulated cable. The detailed circuit of the single module is displayed

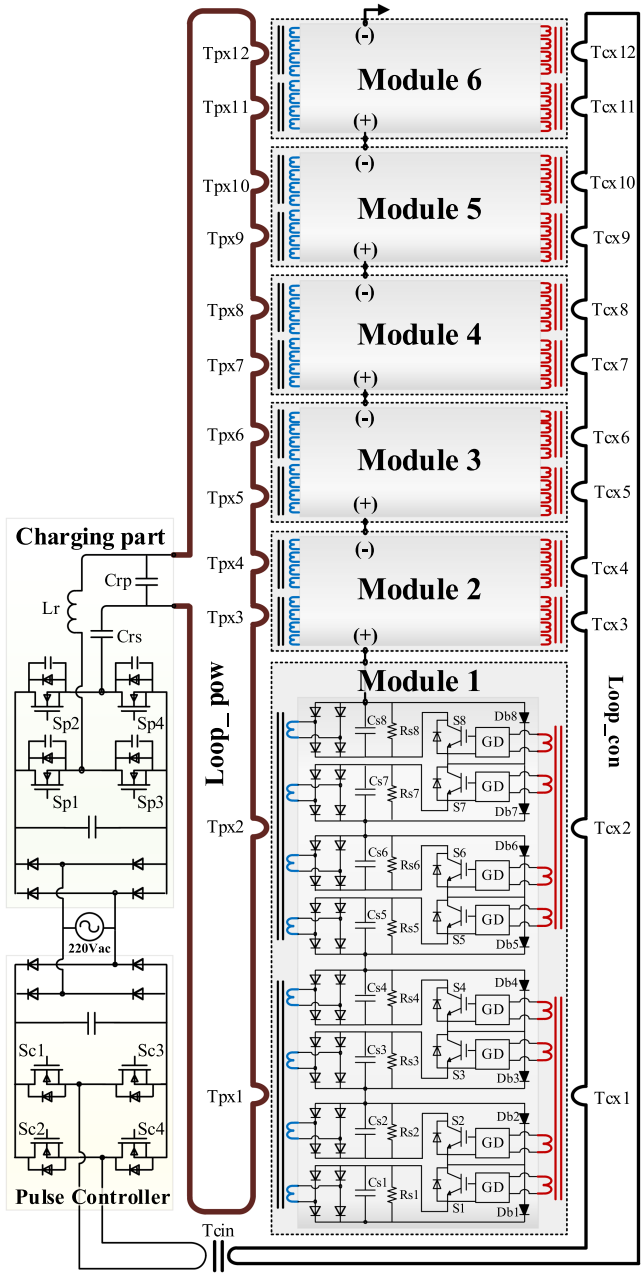

Fig. 1. Total schematic circuit of the designed −40 kV compact pulse modulator.

on the lower-right side of the circuit, and the charging power transformer (Tpx1–Tpx12) is linked to the left side of each module. The four secondary windings of the transformer are connected to the respective storage capacitors (CS1–CS8) via a full-bridge rectifier diode (Dr1–Dr32), and 48 storage capacitors in six modules are charged in parallel to a maximum of 833 V apiece. In addition, storage capacitors are connected in series as the 48 discharge IGBTs (S1–S48) are turned ON, allowing each module to output up to −6.7 kV and the entire module can output a maximum of −40 kV 100 A pulse. A bypass diode (Bb) was connected in parallel with the discharge IGBT. The gate driver is located on the right side of each discharge IGBT. Because the switch must be insulated from the bottom to the top,

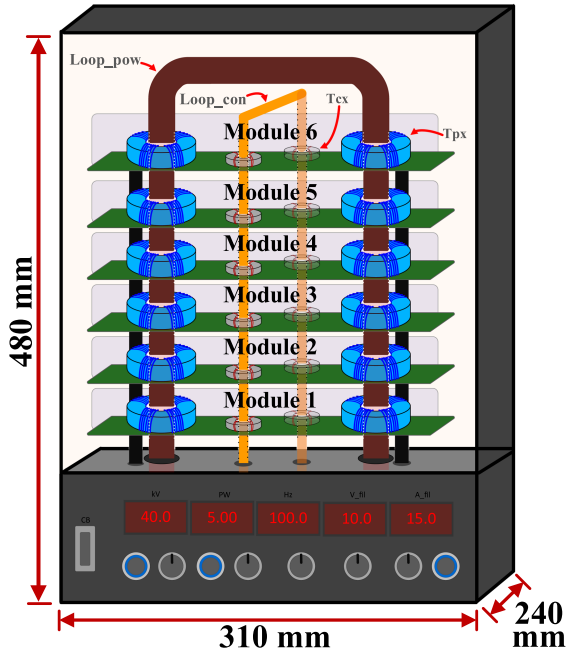

Fig. 2. Overall configuration of the designed pulse power modulator.

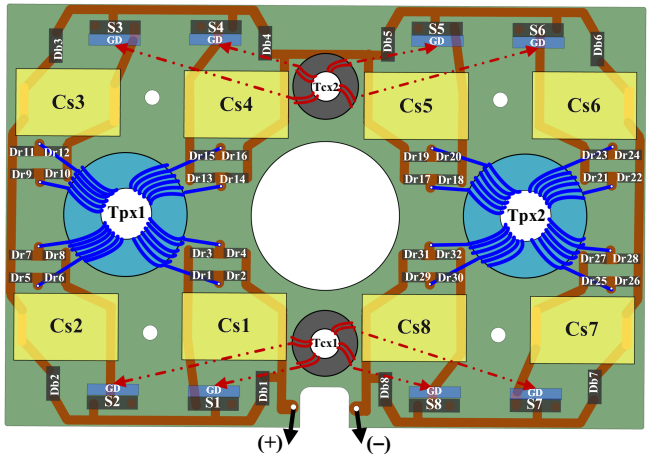

Fig. 3. Single power module configuration (rated output of −6.7 kV and 100 A).

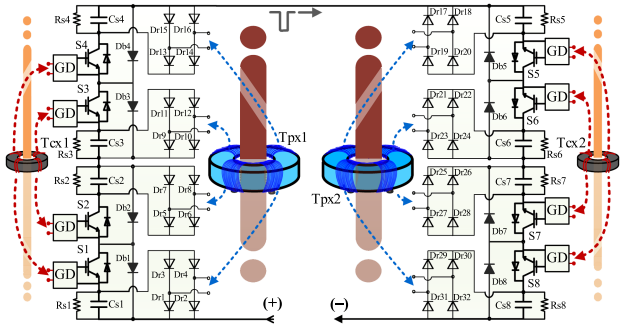

Fig. 4. Schematic circuit of single power module.

the secondary windings of the control transformer (Tcx1–Tcx2) are connected to each of the four gate drivers and are isolated, delivering a synchronized signal to each driver. There were 12 control transformers, and a cable with a dielectric strength of 50 kV was selected for the primary winding (Loop_con) of these transformers. The control loop receives energy in the form of an on–off pulse from the control inverter (Sc1–Sc4) at the bottom left of Fig. 1 to drive 48 high-voltage switches simultaneously. A control isolation transformer (T_{cin}) was located between the control loop and the control inverter. The simplified configuration and dimensions of the high-voltage pulse modulator are shown in Fig. 2. The charging power loop (Loop_pow) and control loop (Loop_con) pass through the power module in an orthogonal loop, and the upper part of the modulator consists of six power modules for generating high-voltage pulses. The lower part consists of a capacitor-charging part and control system. Fig. 3 shows the development of a single module consisting of eight storage capacitors (Cs1–Cs8), eight discharge IGBTs (S1–S8), a gate driver to drive them, 32 rectifier diodes (Dr1–Dr32), and eight bypass diodes (Db1–Db8). In addition, the transformer of the charging power loop (Tpx1–Tpx2) and the transformer of the control loop (Tcx1–Tcx2) were positioned in the cross direction. Fig. 4 shows the schematic circuit of a single power module, in addition to the parallel charging of capacitors and series discharging through IGBT switching ensuring an absolute insulation distance for a high voltage while designing a high-voltage pulse modulator is an important design requirement. In this single module, many isolation designs were implemented based on empirical knowledge of high-voltage isolation. The dielectric strength of typical air at standard atmospheric pressure (1013.25 hPa) is simply defined as 3 kV/mm [16], [17]. While designing various high-voltage power supplies, we experienced that microdischarges such as creepage discharge as well as ambient environments such as humidity and temperature can affect dielectric strength. Therefore, 1 mm or more is considered the minimum insulation distance standard for a voltage of 1 kV. The (+) and (−) terminals, which refer to the output terminals of a single module, are the gap with a potential difference of −6.7 kV, the biggest potential difference inside the module. And, utilizing the gap, the control transformers (Tcx1–Tcx2) with a diameter of 20 mm or more used for driving the four discharge switch gates were efficiently placed. Therefore, an optimized design considering both geometrical characteristics and insulation was possible. Furthermore, the distance between the rectifier diodes Dr17 and Dr31 (as well as Dr3 and Dr13) is the point where a potential difference of 3.4 kV exists, and it is designed to have an insulating distance of 10 mm. The power transformer (Tpx1–Tpx2) has a 1:25 turn ratio, and four secondary windings are used for each core; thus, a total of 100 turns are wound on one toroidal core. However, because a potential difference of 3.4 kV exists between the minimum and maximum voltages of the secondary winding, a winding with a small diameter should be used while ensuring the dielectric strength of the secondary winding. As a result, the secondary winding was made of a Teflon-insulated Litz wire with a dielectric strength of 5 kV. The following is a summary of the insulation design method for such an optimized single module.

1) Optimal design considering both insulation and geometrical characteristics that can efficiently utilize the space of a control transformer (Tcx1–Tcx2) with a diameter of

20 mm for 6.7 kV isolation of the output terminal of a single module.

2) For a 3.4 kV potential difference, ensure a 10 mm insulating distance between rectifier diodes D21 and D17 (similarly between D3 and D5).
3) Considering 3.4 kV insulation, which is the maximum potential difference of 100 turns (25 turns × 4 wires) of the secondary side of the charging transformer (TX1–TX2), four multiwindings, 5 kV insulation, and small-diameter Teflon Litz wire are used.

III. Design of the Proposed Pulse Modulator

A. Parameter Design of Discharging and Charging Part

As the first step in designing a −40 kV semiconductor switch-based modulator, a discharge switch was first selected. The selected switch is an IGBT (FGL40N120AND) rated at 1200 V 64 A. Next, using (1), the number of storage capacitors was selected as 48, considering a 30% margin of the switch rating. Here, V_{o_max} is the maximum output voltage and V_{sw_max} is the rated voltage of the discharge IGBT

$$N_{\text{stor}} \geq \frac{V_{o\_\max}}{V_{\text{SW\_max}} \times 0.7} \tag{1}$$

$$C_{\text{stor}} = \frac{I_{o\_\max} \times PW \times N_{Cs}}{\Delta V_{o\_\max}}. \tag{2}$$

Using (2), the capacitance of the storage capacitor was 15 μF, such that the maximum voltage (V_{o_max}), maximum current (I_{o_max}), and droop rate were within 5% at a pulse width of 4 μs. where N_{cs} denotes the total number of storage capacitors

$$A_e = \frac{V_1 \times 10^4}{2 \times \Delta B \times N_{\text{core}} \times N_1 \times f_{s\_\min}} \tag{3}$$

$$N_2 = \frac{V_o \times N_1 \times N_{\text{core}}}{V_I \times N_{Cs} \times k}. \tag{4}$$

Based on (3), a toroidal core (R50 × 30 × 20, N87) coated with epoxy insulation was chosen for the transformer core in order to reduce the number of turns of the primary wire and the core's area, as well as the inverter MOSFET switching loss. This core has an effective magnetic cross section (Ae) of 2 cm^2 and a magnetic cross section (Ae) of 2 cm^2 and maximum flux density (Bm) of 0.49 T. Based on (4), the number of turns of the four secondary windings wound around 12 cores was chosen to be 25, where N_1 is the number of turns on the primary side, N_{core} is the number of cores, N_{cs} is the number of storage capacitors, and k is a margin proportionality constant with a value of 1.3. The diameter of the primary winding (Loop_pow) of the transformer is 17 mm, and it has a dielectric strength of 100 kV, and the secondary winding has a total of 100 turns on a relatively small toroidal core and has a dielectric strength of 3.4 kV, hence a 1 mm diameter Teflon coated Litz wire (0.07/10) was selected. The minimum switching frequency was 130 kHz, and the maximum switching frequency was 200 kHz, so that the primary turn (N_1) became 1 when the number of cores (N_{core}) of the charging transformer was 12. Furthermore, it operates in a burst mode with discontinuous operation at a switching frequency of 200 kHz or higher owing to the high switching loss due to high-frequency switching during light-load operation. Using the burst mode allows this modulator to operate over a very wide load range. The charging circuit of the designed modulator charges a number of capacitors with a current source based on the *LCC* resonance circuit; therefore, an overcurrent-limiting element such as a diode or resistor is not required between the source and the capacitor. The design details of the resonant parameters of the charger are as follows. The charger implemented the ZVS turn-ON operation of the inverter switch by applying an *LCC* resonant topology based on [18], [19], [20], and [21]. Based on the minimum switching frequency and (5), the parallel resonance frequency fop was selected as 260 kHz

$$P_{tr} = V_{in} \times I_{Ls,\max} \left(1 - \frac{5 f_s}{8 f_{op}}\right) \tag{5}$$

Here, P_{tr} is the maximum power applied to the transformer, and $I_{Ls,\max}$ is the maximum value of the resonance current during the light-load operation. In addition, parallel resonance impedance of 8.2 Ω was obtained through (6), where $V_{Cs,\max}$ is set as $V_{\text{in}}/4$ as the voltage across the series resonant capacitor, and series resonant inductance (Lrs) is 14 μH through (7)–(9)

$$Z_{op} = \frac{V_{Cs,\max} \times 2V_{in}}{I_{Ls,\max}} \tag{6}$$

$$L_r = \frac{Z_{op} \times 2V_{in}}{2\pi \times f_{op}} \tag{7}$$

$$C_{rp} = \frac{L_r}{Z_{op}^2} \tag{8}$$

$$C_{rs} = \frac{\left(\frac{1}{2fs} - \frac{0.375}{f_{op}}\right) \times I_{Ls,\text{peak}}}{2 \times V_{Cs,\text{peak}}} \tag{9}$$

parallel resonant capacitance (Crp) of 200 nF, and series resonant capacitance (Crs) of 15 μF were obtained, respectively.

$$\emptyset_1 = \frac{\mu_o \times \mu_r \times I_{pri} \times A_e}{2\pi r} \tag{10}$$

$$M = N_2 \frac{d\emptyset_{21}}{di_1} = N_1 \frac{d\emptyset_{12}}{di_2}. \tag{11}$$

The primary winding of the transformer uses a thick insulating sheath, because of which the distance (r) between the conductor of winding and the core of the transformer is relatively long. From (10), it observed that the flux generated by the primary winding is relatively small due to the small number of turns and the small cross-sectional area (Ae) of 2 cm^2. Based on (11), it can be observed that the relatively small flux flow in the transformer of this modulator can lead to low mutual inductance, which is defined as the ratio of a time-varying magnetic flux created by one coil being induced into a neighboring second coil. When the primary winding with such a thick insulation sheath is used as a single turn, the proportion of the leakage flux increases significantly. However, the generated leakage inductance is used as the series inductance of the *LCC* resonant converter, which enables a compact capacitor charging part design. A SiC MOSFET (C2M0025120D,1200 V, 60 A) with a low drain-source resistor

TABLE I
DESIGN PARAMETERS AND SELECTED DEVICES OF DEVELOPED MODULATOR

Rated Power, P_{out}	2 kW
Input Voltage, V_{in}	1Ø 220 Vac
DC Link capacitor, C_{dc}	3200 mF
Series Resonant Inductance, L_{rs}	14 μH
Series Resonant Capacitance, C_{rs}	15 µF
Parallel Resonant Capacitance, C_{rp}	100 nF
Snubber capacitor, C_{sn}	8 .2 nF
Switching Frequency, f_S	130 kHz - 200 kHz
Storage capacitor, C_{s1} –C_{s48}	15 µF, 900V, film cap
MOSFET of the charging inverter, S_{p1} –S_{p4}	C2M0025120D (1200V 60A SiC MOSFET)
Rectifier diode, $D_{r1} - D_{r32}$	C4D02120E (1200V 5A SiC DIODE)
Toroidal core of charging transformer, Tpx	R50x30x20, N87 (TDK)
Transformer turns ratio, N1 : N2	1 : 25 (×12 ×4)
Discharging IGBT, ($S_1 - S_{48}$)	FGL40N1FGL40N120 (1200 V/40 A)
Bypass diode, ($D_{b1} - D_{b48}$)	STTH3012 (1200 V/30 A)

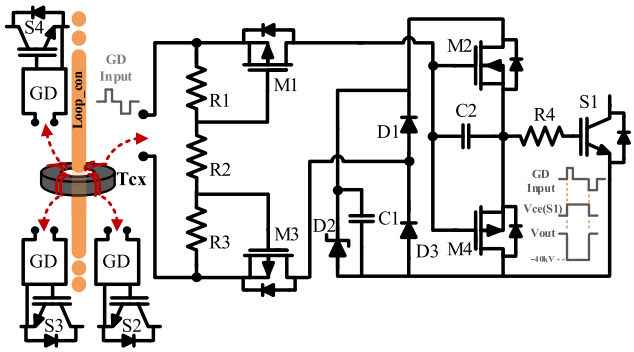

Fig. 5. Gate driving circuit for the main pulse-discharging IGBT and connection structure of four gate drivers through the control loop (Loop_con).

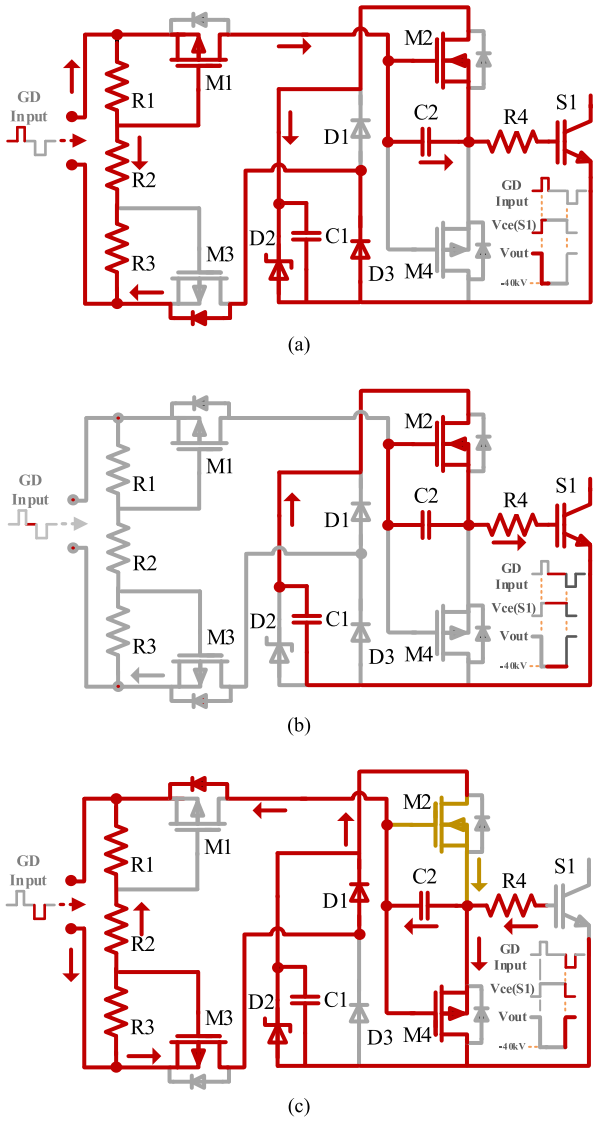

Fig. 6. Operation modes of the proposed gate driver circuit. (a) MODE 1: Turn-ON pulse mode. (b) MODE 2: Turn-ON hold mode. (c) MODE 3: Turn-OFF pulse mode.

in on state was chosen for the charging inverter switches (Sp1–Sp4), and a snubber capacitor of 8.2 nF was used to reduce the turn-off switching loss. Table I outlines the design parameters and selected devices of the developed pulsed-power modulator.

B. Compact Gate Driver Design of Main Discharge Switch

The isolation and synchronized operation of all switches are essential considerations when developing high-voltage modulators. In this modulator, each of the 48 gate drivers is supplied with a synchronized gate signal with an isolated gate driving power. Fig. 5 shows the proposed gate driver circuit, where isolation and synchronization signals are supplied to four gate drivers from each control transformer (Tcx). The voltage input to the gate driver is a simple and short ON/OFF pulse voltage, which can be efficiently controlled by storing the ON/OFF pulse in the capacitor inside the gate driver. Thus, 48 switches can be efficiently controlled, and the size of the control transformer (Tcx) can be minimized. For the control transformer, an R28 × 16 × 13, PC40 toroid core was selected based on (12). Here, V_{in_tcx} is the primary side input voltage of

$$A_e = \frac{V_{in\_tcx} \times T_{\text{off}} \times 10^4}{2 \times \Delta B \times T_{1\_tcx} \times N_{cx2}} \tag{12}$$

the control transformer, T_{off} is the applied off pulse width, saturation magnetic flux density (ΔB) is 0.5, T_{1_tcx} is the number of turns of the primary winding, and N_{cx2} is the number of windings on the secondary of the core.

With short on/off pulses, gate control is simple without using the maximum pulse width directly on the control transformer. Therefore, it was possible to minimize the saturation magnetic flux density of the control transformer. With Fig. 6, the operating principle of the gate driver is as follows.

1) *Mode 1:* Turn-ON mode. When the on-pulse is applied to the gate driver through the control transformer (Tcx), the IGBT (S1) is turned ON by forming a series loop with the antiparallel diodes C2, R4, D3, and M3, together with

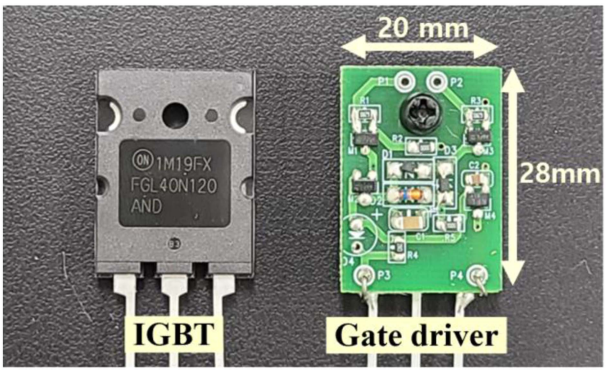

Fig. 7. Photograph comparing the size of the developed gate driver and IGBT (TO-264).

the turn-ON of M1. C2 was connected in series with the IGBT gate to increase the turn-ON speed by reducing the input capacitance of the switch, and the potential of C2 increased.

2) *Mode 2:* Turn-ON hold mode. Without a voltage applied to the gate driver, the charged voltage of C1 is applied to gates *S*1 through *M*2, which is in the turned-ON state, while S1 maintains the turned-ON state. The voltage of C2 was higher than the threshold voltage of M2.
3) *Mode 3:* Turn-OFF mode. When a turn-OFF pulse is applied to the gate driver, M3 is turned ON, a series loop is formed with the antiparallel diodes D1, M2, C2, and M1, and a reverse voltage is applied to C2. At this time, as M_2 is turned OFF, the C1 voltage is no longer connected to the *S*1 gate, and as M4 is turned ON, a discharge path of the charge S1 gate is formed and S1 is quickly turned OFF. Same as the turn-ON modes, C1 was charged.

The designed gate driver is shown in Fig. 7. The gate driver with the same compact size as the IGBT package size of the TO-264 standard was designed.

IV. Design Technique for Improving Stability and Summary

A. Design of Compensation Winding to Equalize Voltage of Multiple Capacitors

It is important and challenging to minimize the power loop of the charging part from the perspective of achieving a compact design of the modulator. In particular, because the primary wire of the charging transformer uses a high-voltage insulated cable with a thick diameter of 17 mm to ensure insulation of −40 kV or more, reducing the number of turns of the primary wire is effective in terms of the compact design of the modulator. However, if the number of turns on the primary side of the transformer passing through multiple cores is reduced, it is difficult to obtain a balanced voltage between the 48 capacitors connected to the secondary wire of the transformer, and an unbalanced capacitor voltage may lead to the breakdown of the discharge switch. In this design of the charging part, a primary wire with a diameter of 17 mm and dielectric strength of 100 kV was selected as a single turn to obtain a compact structure penetrating

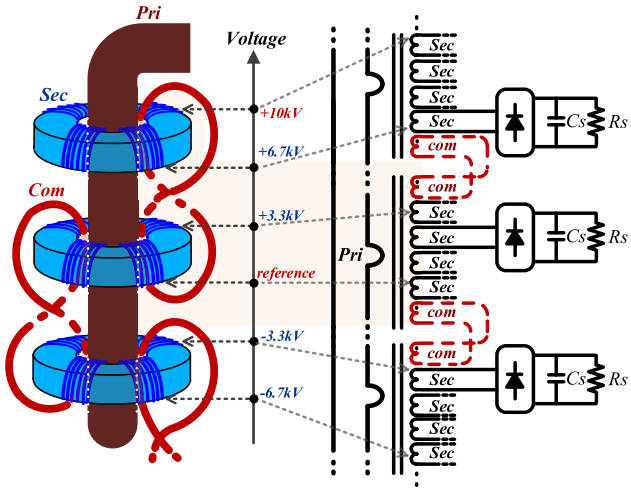

Fig. 8. Configuration and schematic circuit applying the magnetic flux difference compensation strategy of multiple transformers.

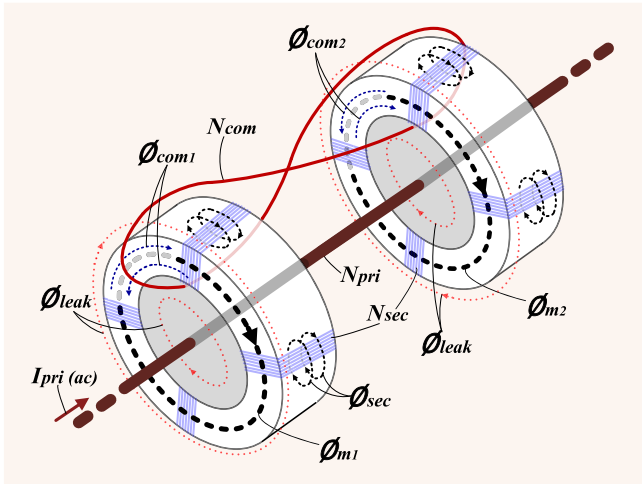

Fig. 9. Configuration and schematic circuit applying the magnetic flux difference compensation strategy of multiple transformers.

12 toroid cores, and a high-voltage insulation of 40 kV was secured. To evenly charge the voltages of the 48 capacitors, magnetic flux compensation circuits between cores were applied to compensate for the difference in leakage inductance that exists in multiple transformers, which is a major problem in capacitor voltage balancing. Thus, equal charging of 48 capacitors was realized.

Fig. 8 shows the configuration and schematic circuit applying the magnetic flux difference compensation strategy for the multiple transformers. The compensating wire is wound on the adjacent transformer and compensates for the difference in the leakage flux between the cores to compensate for the unbalance caused by the leakage inductance difference. Fig. 9 shows the total flux diagram of a multiwinding transformer and compensating winding. Assuming an ideal transformer, the difference in magnetic flux generated by two adjacent cores is equal to the voltage difference between the connected compensating

windings from (13), where $\emptyset_{m1}$ and $\emptyset_{m2}$ are

$$V_{com1}(t) - V_{com2}(t) = N_{com}\left(\frac{d\emptyset_{m1}}{dt} - \frac{d\emptyset_{m2}}{dt}\right) \quad (13)$$

the magnetic fluxes of each core, and if the amount of change of the two magnetic fluxes per unit time varies, the current (I_{com}) due to the voltage difference ($\mathrm{V}_{com1} - \mathrm{V}_{com2}$) of the connected compensating winding occurs. Also, the difference between V_{com1} and V_{com2} (equivalently, the difference between $\Delta\emptyset_{m1}$ and $\Delta\emptyset_{m2}$) determines the direction of I_{com}. And from Lenz's law, just as the direction of the magnetic flux ($\emptyset_m$) generated by the primary side and the direction of the flux ($\emptyset_{sec}$) generated by the secondary side are opposite to each other, the flux ($\emptyset_{com}$) generated by the compensating current also flows in the opposite direction to the magnetic flux ($\emptyset_m$). From (14)

$$\emptyset_{com} = \frac{\mu_o \times \mu_i \times A_e \times N_{com} \times I_{com}}{\ell_c} \quad (14)$$

the compensating flux ($\emptyset_{\mathrm{com}}$) generated by $\mathrm{I}_{\mathrm{com}}$ flows in the opposite direction to the larger $\emptyset_{\mathrm{m}}$ of the two magnetic fluxes ($\emptyset_{\mathrm{m1}}$ and $\emptyset_{\mathrm{m2}}$) and flows in the same direction to the smaller $\emptyset_{\mathrm{m}}$. So, of the two magnetic fluxes ($\emptyset_{\mathrm{m1}}$ and $\emptyset_{\mathrm{m2}}$), the larger $\emptyset_{\mathrm{m}}$ decreases and the smaller $\emptyset_{\mathrm{m}}$ increases. This reduces the difference between the two magnetic fluxes.

The core N87 (TDK) has a cross-sectional area (A_e) of 195.7 mm^2 and a magnetic path length (ℓ_c) of 120.4 mm. In addition, the magnetic permeability (μ_o) of the vacuum is $4\pi \times 10^{-7}[\mathrm{H/m}]$, and the magnetic permeability (μ_r) of the core is 2200. However, an increase in the number of turns of the compensating winding causes a large difference of the compensating voltage ($\mathrm{V}_{com1} - \mathrm{V}_{com2}$) together with an increase in $\emptyset_{com}$, resulting in a large I_{com}. In terms of magnetic flux ($\emptyset_m$) transfer from the primary to the secondary side, an increase in $\emptyset_{com}$ may lead to an increase in the leakage flux, so we achieved the voltage balancing goal while minimizing $\emptyset_{com}$ by using a single-turn compensating winding.

In addition, as shown in Fig. 8, in the high voltage design of the multimodule structure, the compensation winding should have maximum insulation of 10 kV or more, and an insulated cable of 20 kV was selected. Another technique to balance voltage is the use of capacitor parallel resistors (Rs1–Rs8) [22], [23]. When the 48 storage capacitors are fully charged through the charging current of the current source, the impedance of the charged capacitor may be different due to a small manufacturing tolerance and self-discharge. To minimize the effect of the difficult-to-control tolerance and leakage current of the capacitor, a large 180 kΩ parallel resistor is installed across each capacitor based on (15)

$$R_s = \frac{N_{\mathrm{cell}} \times V_{cs} - V_{\mathrm{total}}}{I_{c\_\mathrm{leak}}}. \quad (15)$$

Here, N_{cell} denotes the number of capacitor stacks used, V_{cs} denotes the maximum voltage that can be applied to the capacitor, V_{total} denotes the sum of the stacked capacitor voltages, and I_{c_leak} denotes the leakage current of the capacitor. Through this simple compensation method, equal voltage charging within 5% between the 48 storage capacitors was realized without the need for a separate control circuit for balancing.

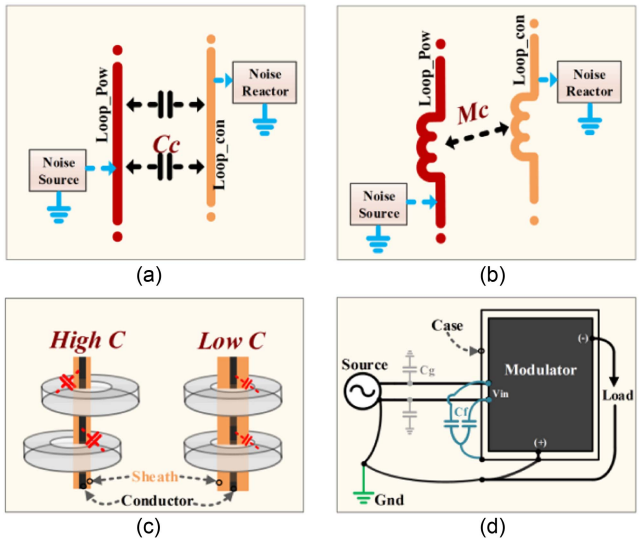

Fig. 10. Design strategies for reducing the effect of high voltage electric field noise. (a) Capacitive coupling. (b) Inductive coupling. (c) Difference in capacitance according to wire sheath diameter. (d) Capacitor (Cf) added between Input – Gnd.

B. Design Strategies for Reducing the Effect of High Voltage Electric Field Noise

The high-voltage pulse voltage, which has a very high-frequency characteristic, causes unintended malfunctions, such as high-voltage electric field noise, especially when designing a compact modulator. In this study, a technique to improve transient immunity, such as a parasitic parameter reduction design, was applied to this modulator to reduce the adverse effects of high-voltage electric field noise as follows.

1) Minimizing capacitive coupling and inductive coupling of the power loop and control loop: The explanation of capacitive coupling and inductive coupling of two parallel lines is shown in Fig. 10(a) and (b), where Cc is the coupling capacitance and *Mc* is the coupling mutual inductance. In this study, as a strategy to minimize the *Cc* and *Mc* of two adjacent lines, the power and control loops were designed in an orthogonal loop structure.
2) Fig. 11 shows the parasitic capacitance of the control transformer. In this design, the parasitic capacitance (C23) of the control transformer (Tcx) and the parasitic capacitance (C12) of the isolating transformer (Tcin) were configured in series to reduce the capacitance. When the capacitance decreases when outputting a high voltage pulse with a high-frequency characteristic, by increasing the impedance of the capacitance, parasitic malfunction of the pulse controller located in the low voltage section, and its low power devices due to high voltage pulse noise with high-frequency components can be suppressed.
3) Setting of equal spacing between the core of the control transformer and the primary winding: The control transformer sheath diameter was increased to reduce the error of parasitic capacitance for each core caused by unequal position between the core and conductor of the control

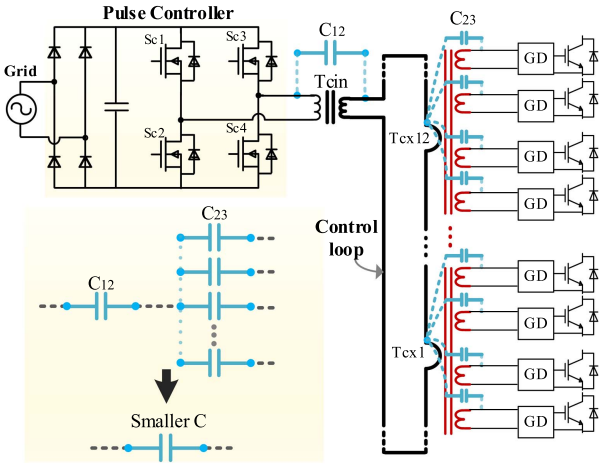

Fig. 11. Diagram of parasitic capacitance of control transformer.

TABLE II
DESIGN SPECIFICATIONS OF DEVELOPED MODULATOR

Input Voltage	1Ø 220 Vac
Maximum Peak Power	4 MW
Maximum output voltage	-40 kV
Maximum output current	100 A
Range of Pulse width	1 μs ~ 10 μs
Maximum repetition rate	1 kHz
Modulator size (W × D × H)	**310 mm × 480 mm × 240 mm**
Modulator volume	**36 Liters**
Modulator weight	**16.4 kg**
Peak power density	**111 kW/L**

transformer which can cause synchronization errors of the gate drivers connected to each transformer.

4) Addition of filter capacitor attached between line and ground: When outputting high-voltage pulses, there is also an invisible weak point between the input line and ground. Source-side instability adversely affects the signal levels. As a mitigation measure, the filter capacitor (Cf) between modulator input line and ground was added, a modulator input and a Gnd capacitor were added, which increased the capacitance (Cg) between the source and the Gnd. In this design, a 500 nF film capacitor was added between the input and Gnd.

C. Summary and Distinctive Features of Modulator Design

Fig. 12 presents the solid-state pulsed-power modulator developed in this study and the measured dimensions, which were manufactured in a highly compact size of 36 L. A compact modulator (310 (W) mm × 480 (H) mm × 240 (D) mm) with a high peak power density of 111 kW/L was designed. Table II shows the design specifications of the developed modulator.

The distinctive features of the proposed compact pulse modulator are as follows.

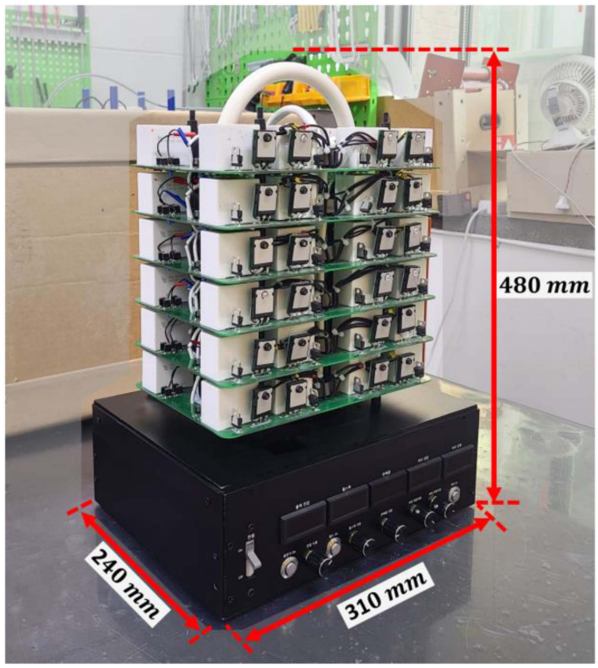

Fig. 12. Designed −40 kV compact modulator (with dimensions marked).

1) A highly simple isolated synchronous control circuit: Each power module has two toroidal transformers with four multiwinding to further simplify the control circuit. Also, it was developed with a simple layout, with the primary side of each control transformer being a single-turn control loop that passes through six modules. Unlike other current source gate drivers [24], [25], this circuit can control the output pulse width in a range from 1 to 10 μ s remaining relatively unaffected by the transformer saturation by using an on–off pulse with a short pulse width. Here, 48 switches are synchronized and isolated under 40 kV high voltage while using short on-and-off bipolar pulses as trigger signals and power sources without the need for additional gate driving power. It is also highly effective at lowering system volume and cost since it does not utilize optical signal control, which needs an independent dc source for each switch.
2) Modular cell-based multimodule penetrating orthogonal loop structure: In the control loop technique that enables the development of modular-cell based pulse modulator [13] with minimum size, stable output without unintended parasitic malfunction is a challenging area and is based on practical design capability. With the suggested orthogonal loop structure, it is possible to reduce the coupling inductance and capacitance between the charging loop and the control loop. Additionally, without horizontal wiring, the high-voltage cable passed through the entire module to minimize the line inductance of the two loops.
3) Highly compact high-voltage pulse modulator design: Based on (3), since it is more efficient to use a multicore with a smaller size than a single-core with a larger size in a multimodule structure. Considering the switching

TABLE III
COMPARISON OF PULSE POWER MODULATORS FOR MAGNETRON APPLICATION

	This work	[14]	[26]	[27]	[28]	[29]
Maximum Peak Power	4 MW	6 MW	4 MW	6.2 MW	6 MW	6.2 MW
Maximum output voltage	40 kV	40 kV	40 kV	52 kV	50 kV	52 kV
Maximum output current	100 A	150 A	100 A	120 A	120 A	120 A
Modulator volume	36 Liters	92 Liters	81.6 Liters	133 Liters	≥ 200 Liters	≥ 200 Liters
Peak power density	111 kW/L	65 kW/L	49 kW/L	46 kW/L	≤ 30 kW/L	≤ 31 kW/L

frequency, the number of cores, and the diameter of the insulated cable used, a toroidal core (R50 × 30 × 20) with a small effective magnetic cross-section (Ae) of 2 cm^2 was placed in each of the six modules. In addition, by using a 100 kV insulated cable with a diameter of 17 mm as the primary side of the single-turn transformer, insulation for 6 modules and the transfer of charging power to the secondary side were simply realized. Based on such a simple charge and discharge structure and a compact gate driver design, the highly compact and lightest design among the pulse power devices [14], [26], [27], [28], [29] in Table III was realized for driving magnetrons with peak power of MW class including commercial modulators (modulator volume of 36 L, weight of 16.4 kg and peak power density of 111 kW/L).

4) Proposed simple multi-capacitor voltage balancing: Despite the fact that a highly compact design of the modulator is possible based on the structure in which the single-turn winding of the charging part passes through multiple cores, the balancing error of 48 capacitors occurs owing to the difference in magnetic flux in multiple cores and multiple windings and manufacturing tolerance. As a strategy to solve this problem, a compensation winding to compensate the magnetic flux imbalance between multiple cores was first applied, and the design of the compensation winding proposed in consideration of a simple magnetic flux analysis and insulation technique is described in this article. In addition, when the charging current of the current source charges 48 storage capacitors, 180 kΩ parallel resistors were installed at both ends of each capacitor to minimize the effect of small manufacturing tolerance on the capacitors. Based on this, voltage balancing within 5% of 48 capacitors was achieved.

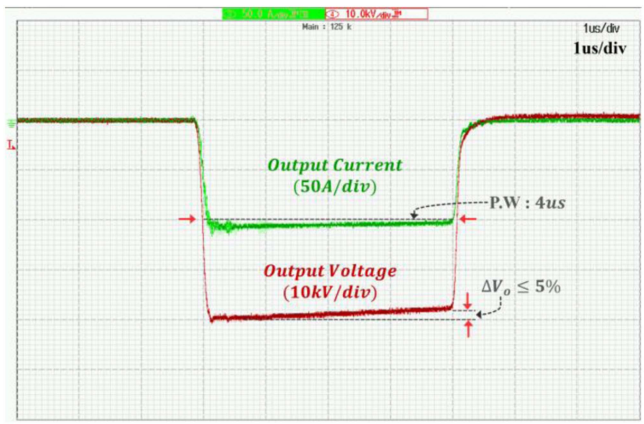

Fig. 13. Output pulse voltage and current waveform at the rated conditions of −40 kV and 100 A [10 kV/div, 50 A/div].

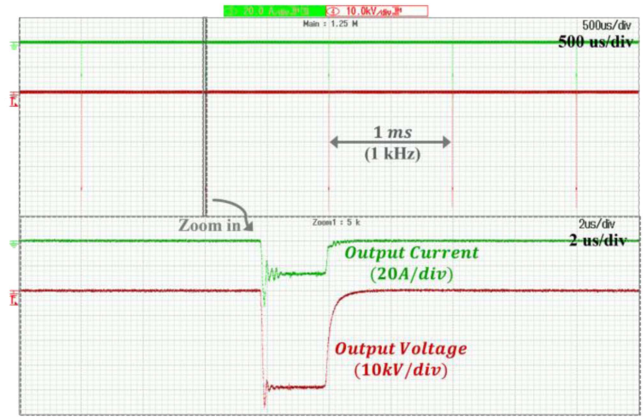

Fig. 14. Experimental waveforms of the −40 kV pulse output voltage during operation at 1 kHz maximum repetitive rate operation [10 kV/div, 20 A/div].

V. EXPERIMENTAL RESULTS

The experiment was performed under a 400 Ω noninductive resistive load (ET-150, 3RLab) to output −40 kV, 100 A under the rated condition of the modulator. Fig. 13 shows the output waveform of the rated voltage and current of the designed high-voltage pulse modulator, which outputs a negative pulse and a pulse of −40 kV, 100 A, and a pulse width of 4 μs. Under these conditions, the droop rate of the output voltage is less than 5%. Fig. 14 shows that the modulator's maximum repetition rate of 1 kHz was achieved at a pulse voltage of −40 kV, and the experiment was performed under the condition of an average output of 2 kW. Fig. 15 shows the switching loss of 7.5 mW of the discharge switch (S_1) under output condition of −40 kV, 100 A, single pulse output of 4 μs, and the switching loss of 937.5 mW at a 125 Hz repetition rate (2 kW rated output). Moreover, the conduction loss was 130 mW under the 2 kW output condition of IGBT saturation voltage of 2.6 V, 100 A, 4 μs, and 125 Hz; therefore, the total switching loss at the rated output was approximately 1 W. Therefore, it was confirmed that the loss of the IGBT at the rated output was 1% of the rated 200 W ($T_c = 100$ °C) of the IGBT dissipation power. Fig. 16 shows the experimental waveform in which the pulse width was flexibly varied from 2 to 10 μs under a condition of −40 kV voltage and 100 A current. Here, the relationship between the increase

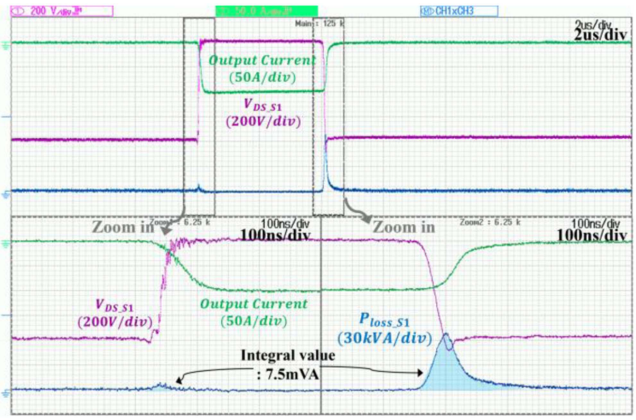

Fig. 15. Switching loss waveform of discharge switch in single pulse output [200 V/div, 50 A/div, 30kVA/div].

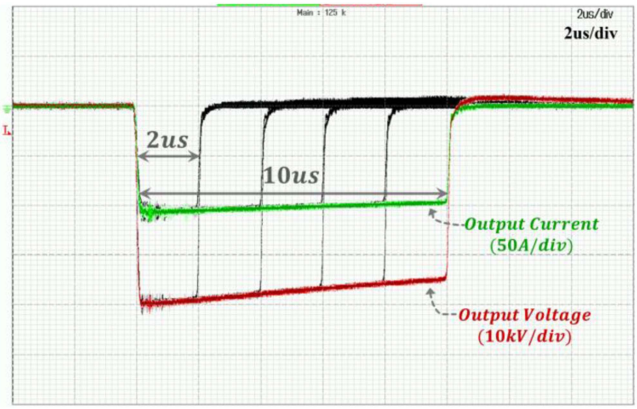

Fig. 16. Experimental waveforms of variable pulse width operation with variable 2–10 μs pulse width. [10 kV/div, 50 A/div].

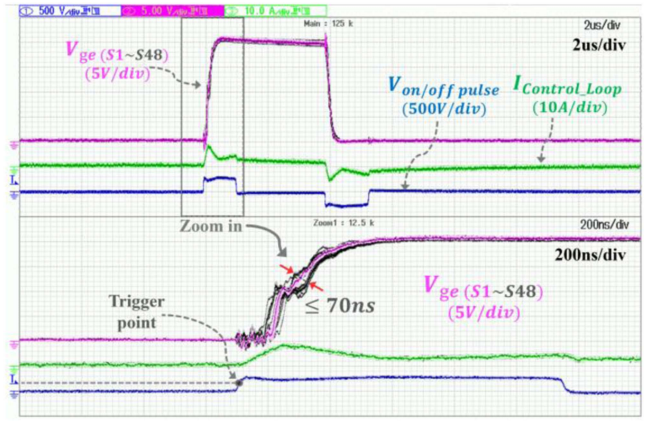

Fig. 17. Waveform of the synchronous gate voltage for each of 48 main IGBT [5 V/div] current of control loop [10 V/div] and on/off pulse output voltage of the pulse controller [500 V/div].

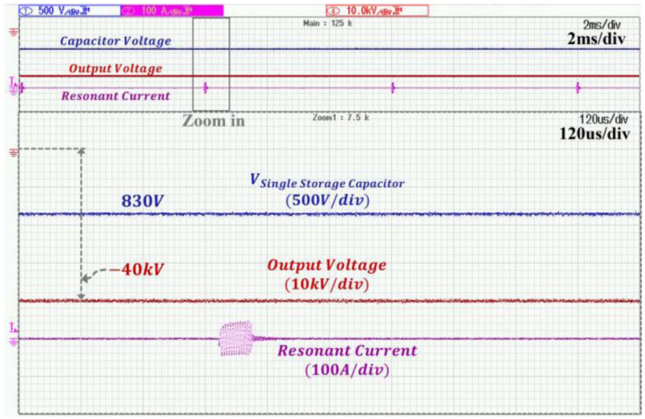

Fig. 18. Waveform of −40 kV dc output test result [10 kV/div], single storage capacitor voltage [500 V/div] and charging resonant current [100 A/div].

in pulsewidth and the droop rate is determined according to (2), and as the storage capacitor increases, the droop rate can be decreased. Therefore, we decided to use 48 storage capacitors so that the droop rate is within 5% at the maximum pulse width of 4 μs, which is the required specification of the 1.7 MW X-band Magnetron (L6170, L3) applied to the modulator. Fig. 17 depicts the experimental results for the synchronization characteristics of the gate voltages of the 48 discharge switches. After using the rising edge of the on-pulse of the output voltage of the pulse controller at the bottom as a trigger signal, the 48 IGBTs were measured by zooming in, and it was confirmed that they had a synchronization error within 70 ns. Fig. 18 depicts the results of the dc output of the modulator. The voltage required for repetitive pulsed breakdown is typically 20% greater than voltages in dc breakdown condition [30]. Therefore, by connecting the collector-emitter of 48 discharge switches, the entire module is connected in series, and operated for about 10 min at 40 kV dc output condition. Pulse output is performed if the result of the harshest −40 kV dc output experiment is not abnormal. This process verifies the isolation between each module of the modulator. Figs. 19 and 20 depict the voltage distribution waveforms for each power module without and with compensation winding circuit, respectively. The maximum

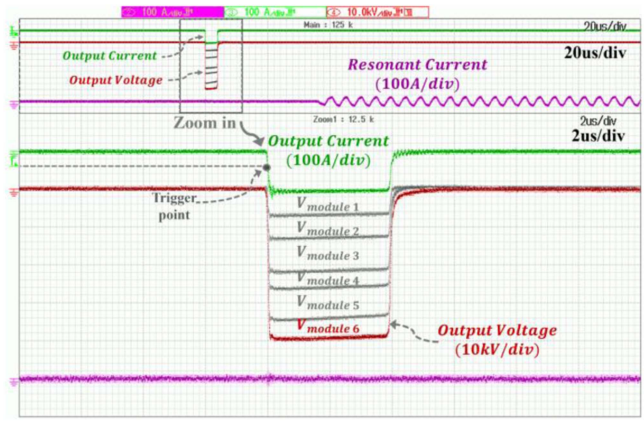

Fig. 19. Voltage distribution waveform for each power module without compensation winding [10 kV/div], Pulse output current [100 A/div] and charging resonant current [100 A/div].

voltage balancing error for each module, based on 6.7 kV, is 29% when compensating winding is not applied. In comparison to this, applying it resulted in a voltage balancing error rate of less than 5%. By triggering a negative output current with a falling edge, the voltage from the output voltage of module 1

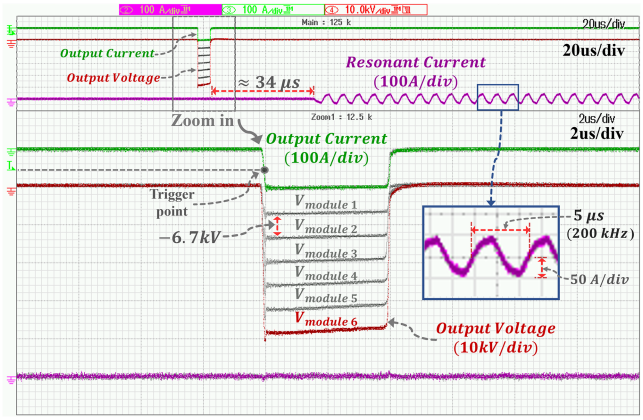

Fig. 20. Voltage distribution waveform for each power module with compensation winding [10 kV/div], Pulse output current [100 A/div] and charging resonant current [100 A/div].

to that of module 6 was measured using a high-voltage probe (P6015A, Tektronix). The purple color represents the resonance current in the zoom-out waveform at the top, and it shows a discontinuous operation (burst mode) to limit the high switching frequency at a light load. After the pulse discharge, the storage capacitor voltage was sensed to resume the charging operation within 34 μs, and the maximum switching frequency was limited to 200 kHz. The enlarged waveform of the resonance current is shown in the lower-right corner.

VI. Conclusion

The modulator outputs −40 kV pulses based on the modular cell scheme and is designed efficiently by arranging the control loop and capacitor charging loop in orthogonal directions to supply isolation and synchronization signals to 48 IGBT gates in a simple manner. In addition, in the capacitor charging structure using multiple transformers, a compensation circuit was applied to solve the uneven charging between capacitors owing to the difference in the magnetic flux generated when the single-turn primary winding was utilized, and the charging balancing rate of 48 capacitors was within 5%. Based on the practical design of the modulator and a simple and reliable gate driving circuit design, a modulator with a highly compact size (310 (W) mm × 480 (H) mm × 230 (D) mm) and a very high peak power density of 111 kW/L was designed. The developed modulator was tested under a high-voltage noninductive resistive load, and it was tested under various conditions, such as a maximum output voltage of −40 kV, a maximum output current of 100 A, a pulse width of 2–10 μs, a maximum repetition rate of 1 kHz, and a voltage capacitor voltage balancing test within 5%. The high-voltage insulation reliability of the proposed modulator and its applicability to magnetron loads were verified by outputting a stable pulse voltage.

References

[1] A. S. Alimov et al., "A compact industrial high-current continuous wave electron LINAC," in *Proc. Part. Accel. Conf.*, 1999, vol. 4, pp. 2555–2557, doi: 10.1109/PAC.1999.792774.

[2] M. N. Martins and T. F. Silva, "Electron accelerators: History, applications, and perspectives," *Radiat. Phys. Chem.*, vol. 95, pp. 78–85, Feb. 2014.

[3] S. Das, R. Krishnan, A. P. Bhagwat, and S. N. Pethe, "LINAC for medical applications," in *Proc. IEEE Int. Vac. Electron. Conf.*, 2009, pp. 283–284, doi: 10.1109/IVELEC.2009.5193402.

[4] S. H. Kim et al., "Development of a compact X-band linear accelerator system mounted on an O-arm rotating gantry for radiation therapy," *Rev. Sci. Instrum.*, vol. 92, no. 2, Feb. 2021, Art. no. 024103, doi: 10.1063/5.0030271.

[5] J. J. Lagendijk, B. W. Raaymakers, and M. van Vulpen, "The magnetic resonance imaging-LINAC system," *Seminars Radiat. Oncol.*, vol. 24, no. 3, pp. 207–209, Jul. 2014, doi: 10.1016/j.semradonc.2014.02.009.

[6] T. Krian, S. N. Pethe, and R. Krishnan, "Development of a pulse modulator to drive 6.19 MW klystron for 15 MeV electron LINAC," in *Proc. Int. Symp. Discharges Elect. Insul. Vac.*, 2014, pp. 569–571.

[7] N. Carleto, C. R. B. Miranda, and C. C. Motta, "Design of an pulse-forming network for driving high power magnetron," in *Proc. 11th Simpósio Brasileiro de Microondas e Optoeletrônica e 6°Congresso Brasileiro de Eletromagnetismo*, Aug. 2004, pp. 16–19.

[8] S. Castagno, R. D. Curry, and E. Loree, "Analysis and comparison of a fast turn-on series IGBT stack and high-voltage-rated commercial IGBTS," *IEEE Trans. Plasma Sci.*, vol. 34, no. 5, pp. 1692–1696, Oct. 2006.

[9] J. A. A. Casey, M. P. J. Gaudreau, M. Kempkes, J. P. Eichner, S. J. Gold, and R. F. Koontz, "Solid-state hybrid modulator for the next linear collider," in *Proc. 14th IEEE Int. Pulsed Power Conf. Dig. Tech. Papers*, 2003, vol. 1, pp. 543–546, doi: 10.1109/PPC.2003.1277769.

[10] R. Cassel, "The evolution of pulsed modulators from the Marx generator to the solid state Marx modulator and beyond," in *Proc. IEEE Int. Power Modulator High Voltage Conf.*, 2012, pp. 9–13.

[11] R. L. Cassel, "An all solid state pulsed Marx type modulator for magnetrons and klystrons," in *Proc. IEEE Pulsed Power Conf.*, 2005, pp. 836–838, doi: 10.1109/PPC.2005.300791.

[12] H. J. Lim et al., "Solid-state pulse modulator using Marx generator for a medical LINAC electron-gun," *J. Instrum.*, vol. 11, Apr. 2016, Art. no. P04003, doi: 10.1088/1748-0221/11/04/P04003.

[13] S.-B. Ok, H.-J. Ryoo, S.-R. Jang, S.-H. Ahn, and G. Goussev, "Design of a high-efficiency 40-kV 150-A 3-kHz solid-state pulsed power modulator," *IEEE Trans. Plasma Sci.*, vol. 40, no. 10, pp. 2569–2577, Oct. 2012.

[14] S.-M. Park, S.-H. Song, H.-B. Jo, W.-C. Jeong, S.-R. Jang, and H.-J. Ryoo, "Solid-state pulsed power modulator for 9.3 GHz 1.7 MW X-band magnetron," *IEEE Trans. Ind. Electron.*, vol. 68, no. 2, pp. 1148–1154, Feb. 2021, doi: 10.1109/TIE.2020.2967728.

[15] H.-B. Jo, S.-H. Song, S.-H. Lee, and H.-J. Ryoo, "MOSFET gate driver circuit design for high repetitive (200 kHz) high voltage (10 kV) solid-state pulsed-power modulator," *IEEE Trans. Power Electron.*, vol. 36, no. 9, pp. 10461–10469, Sep. 2021, doi: 10.1109/TPEL.2021.3062612.

[16] J. L. R. Hayden, "The dielectric strength of the vacuum: Electrostatic ionization gradient of metal electrodes," *J. Amer. Inst. Elect. Engineers*, vol. 41, no. 11, pp. 852–853, Nov. 1922, doi: 10.1109/JoAIEE.1922.6591649.

[17] D. Rodriguez, R. S. Gorur, and P. M. Hansen, "Combined effects of humidity and frequency on the dielectric strength of air for VLF applications," in *Proc. Annu. Rep. Conf. Elect. Insul. Dielectric Phenomena*, 2008, pp. 611–614, doi: 10.1109/CEIDP.2008.4772881.

[18] S.-R. Jang, C.-H. Yu, and H.-J. Ryoo, "Trapezoidal approximation of LCC resonant converter and design of a multistage capacitor charger for a solid-state Marx modulator," *IEEE Trans. Power Electron.*, vol. 33, no. 5, pp. 3816–3825, May 2018, doi: 10.1109/TPEL.2017.2716975.

[19] J.-B. Ahn, S.-H. Song, and H.-J. Ryoo, "Design and implementation of 3-kW simmer and 30-kV DC trigger power supply system for driving xenon flash lamps in large-area processes," *IEEE Trans. Ind. Electron.*, vol. 69, no. 12, pp. 11999–12008, Dec. 2022, doi: 10.1109/TIE.2021.3128898.

[20] J. M. Alonso, C. Blanco, E. Lopez, A. J. Calleja, and M. Rico, "Analysis, design, and optimization of the LCC resonant inverter as a high-intensity discharge lamp ballast," *IEEE Trans. Power Electron.*, vol. 13, no. 3, pp. 573–585, May 1998, doi: 10.1109/63.668122.

[21] S.-H. Ahn, S.-R. Jang, and H.-J. Ryoo, "High-efficiency bidirectional three-phase LCC resonant converter with a wide load range," *IEEE Trans. Power Electron.*, vol. 34, no. 1, pp. 97–105, Jan. 2019, doi: 10.1109/TPEL.2018.2815078.

[22] M. Uno, "Single-and double-switch cell voltage equalizers for series connected lithium-ion cells and supercapacitors," in *Proc. 31st Int. Telecommun. Energy Conf.*, 2009, pp. 1–4, doi: 10.1109/INTLEC.2009.5351990.

[23] Aluminum electrolytic capacitor application guide, CDM Cornell Dubilier, 2011. [Online]. Available: http://www.cde.com/resources/catalogs/AEappGUIDE.pdf

[24] Q. Wu, Q. Wang, J. Zhu, and X. Lan, "Dual-channel push–pull isolated resonant gate driver for high-frequency ZVS full-bridge converters," *IEEE Trans. Power Electron.*, vol. 34, no. 5, pp. 4019–4024, May 2019, doi: 10.1109/TPEL.2018.2873192.
[25] Y. Shang, S. Zhao, Y. Fu, B. Han, P. Hu, and C. C. Mi, "A lithium-ion battery balancing circuit based on synchronous rectification," *IEEE Trans. Power Electron.*, vol. 35, no. 2, pp. 1637–1648, Feb. 2020, doi: 10.1109/TPEL.2019.2917390.
[26] Productsheet of M-SERIES M050-i, ScandiNova Systems AB, Uppsala, Sweden, 2017. [Online]. Available: https://scandinovasystems.com/pulse-modulator/m-series/m050-i
[27] B. N. Lee et al., "Status of KAERI 6 MeV 9.3 GHz X-band electron LINAC for cancer treatment system," in *Proc. 5th Int. Part. Accel. Conf.*, 2014, Paper no. WEPRO090, doi: 10.18429/JACoW-IPAC2014-WEPRO090.
[28] H. J. Lim, D. H. Jeong, M. W. Lee, and S. C. Ro, "Design of a 6-MW solid-state pulse modulator using Marx generator for the medical LINAC," *IEEE Trans. Plasma Sci.*, vol. 45, no. 10, pp. 2734–2738, Oct. 2017.
[29] P. J. Rathod, V. P. Anitha, G. V. Prakash, and Z. H. Sholapurwala, "A magnetron pulsed modulator for microwave plasma interaction studies," in *Proc. IEEE Pulsed Power Conf.*, 2015, pp. 1–4, doi: 10.1109/PPC.2015.7296885.
[30] J. J. Mankowski, "High-voltage subnanosecond dielectric breakdown," Ph.D. dissertation, Dept. Elect. Eng., Texas Teck Univ., Lubbock, TX, USA, 1997.
[31] E. P. Wigner, "Theory of traveling-wave optical laser," *Phys. Rev.*, vol. 134, pp. A635–A646, Dec. 1965.

Hyun-Bin Jo received the B.S. degree in electronic engineering from the Catholic University, Bucheon, South Korea, in 2016. He is currently working toward the M.S. and Ph.D. degrees with the Department of Energy Engineering, Chung-Ang University, Seoul, South Korea.

His current research interests include soft-switched resonant converter applications and high-voltage pulsed-power supply systems.

Jae-Beom Ahn received the B.S. degree in electronic engineering from the Kook-Min University, Seoul, South Korea, in 2019. He is currently working toward the M.S. and Ph.D. degrees in energy system engineering from the Chung-Ang University, Seoul, South Korea.

His current research interests include power electronics and high-voltage pulse power systems.

Woo-Cheol Jeong received the B.S. degree in energy systems engineering, in 2019, from the Chung-Ang University, Seoul, South Korea, where he is currently working toward the Integrated M.S. and Ph.D. degrees in energy systems engineering.

His research interests include soft-switched resonant converter applications and high voltage pulsed-power supply systems.

Joo-Young Lee received the B.S. degree, in 2019, from the Department of Nursing, Chung-Ang University, Seoul, South Korea, where she is currently working toward the Integrated M.S. and Ph.D. degrees in energy systems engineering.

Her research interests include high voltage pulsed-power supply systems and soft-switched resonant converter applications.

Min-Kyu Choi received the B.S. degree in energy systems engineering from the Chung-Ang University, Seoul, South Korea, in 2022, where he is currently working toward the M.S. degree in energy systems engineering.

His research interests include high-voltage pulsed-power supply systems and resonant converter applications for light sintering systems.

Hong-Je Ryoo (Senior Member, IEEE) received the B.S., M.S., and Ph.D. degrees in electrical engineering from Sungkyunkwan University, Seoul, South Korea, in 1991, 1995, and 2001, respectively.

From 2004 to 2005, he was a Visiting Scholar with WEMPEC, University of Wisconsin-Madison, Madison, WI, USA. From 1996 to 2015, he joined the Electric Propulsion Research Division as a Principal Research Engineer, the Korea Electrotechnology Research Institute, Changwon, South Korea, where he was a Leader with the Pulsed Power World Class Laboratory, a director of Electric Propulsion Research Center. From 2005 to 2015, he was a Professor with the Department of Energy Conversion Technology, University of Science and Technology, Deajeon, South Korea. In 2015, he joined the School of Energy Systems Engineering, Chung-Ang University, Seoul, where he is currently a Professor. His current research interests include pulsed-power systems and their applications, as well as high-power and high-voltage conversions.

Prof. Ryoo is currently the Vice President of Cooperation and Chairperson of High Voltage and Pulsed Power Application Research Council of the Korean Institute of Power Electronics and the Vice President of the Korean Institute of Illuminations and Electrical Installation Engineers.